RESEARCH ARTICLE

Key Points:
- A generic InSAR atmospheric correction model with global availability at any time and in all weathers is developed
- High spatial resolution ECMWF model and GPS estimates are integrated to decouple the tropospheric stratification and turbulence
- Performance indicator metrics for quality control and model applicability are developed

Correspondence to:
Z. Li,
zhenhong.li@newcastle.ac.uk

Generic Atmospheric Correction Model for Interferometric Synthetic Aperture Radar Observations

Chen Yu[1] (iD), Zhenhong Li[1] (iD), Nigel T. Penna[1] (iD), and Paola Crippa[1,2] (iD)

[1]School of Engineering, Newcastle University, Newcastle upon Tyne, UK, [2]Department of Civil and Environmental Engineering and Earth Sciences, University of Notre Dame, Notre Dame, IN, USA

Abstract For mapping Earth surface movements at larger scale and smaller amplitudes, many new synthetic aperture radar instruments (Sentinel-1A/B, Gaofen-3, ALOS-2) have been developed and launched from 2014–2017, and this trend is set to continue with Sentinel-1C/D, Gaofen-3B/C, RADARSAT Constellation planned for launch during 2018–2025. This poses more challenges for correcting interferograms for atmospheric effects since the spatial-temporal variations of tropospheric delay may dominate over large scales and completely mask the actual displacements due to tectonic or volcanic deformation. To overcome this, we have developed a generic interferometric synthetic aperture radar atmospheric correction model whose notable features comprise (i) global coverage, (ii) all-weather, all-time useability, (iii) correction maps available in near real time, and (iv) indicators to assess the correction performance and feasibility. The model integrates operational high-resolution European Centre for Medium-Range Weather Forecasts (ECMWF) data (0.125° grid, 137 vertical levels, and 6-hr interval) and continuous GPS tropospheric delay estimates (every 5 min) using an iterative tropospheric decomposition model. The model's performance was tested using eight globally distributed Sentinel-1 interferograms, encompassing both flat and mountainous topographies, midlatitude and near polar regions, and monsoon and oceanic climate systems, achieving a phase standard deviation and displacement root-mean-square (RMS) of ~1 cm against GPS over wide regions (250 by 250 km). Indicators describing the model's performance including (i) GPS network and ECMWF cross RMS, (ii) phase versus estimated atmospheric delay correlations, (iii) ECMWF time differences, and (iv) topography variations were developed to provide quality control for subsequent automatic processing and provide insights of the confidence level with which the generated atmospheric correction maps may be applied.

1. Introduction

Interferometric synthetic aperture radar (InSAR) has been demonstrated as a powerful tool for mapping the Earth's surface movements. The tremendous development of InSAR missions (e.g., Sentinel-1A/1B, ALOS-2, TerraSAR-X/TanDEM-X, COSMO-SkyMED, RADARSAT-2, and Gaofen-3) in recent years facilitates the study of smaller amplitude ground deformation using longer time series and over greater spatial scale (Hooper et al., 2012; Massonnet et al., 1994; Simons & Rosen, 2007). However, the accuracy of InSAR-derived surface displacements is substantially affected by the spatial-temporal variations of atmospheric (tropospheric) water vapor, which can cause errors comparable in magnitude to those associated with crustal deformation (Hanssen, 1998; Wadge et al., 2002; Williams et al., 1998). Zebker et al. (1997) reported that typical spatial and temporal changes of 20% in water vapor can lead to 10- to 14-cm errors in SIR-C/X-SAR derived displacements, which is large enough to mask actual ground motions caused by a landslide (Luzi et al., 2004), urban subsidence (Crosetto et al., 2002), and permafrost (Short et al., 2014). Nonsteady deformation is hard to distinguish from atmospheric errors, which also makes it challenging to detect time varying processes such as creep (e.g., Hussain et al., 2016; Jolivet et al., 2015) or slow slip events (Bekaert et al., 2016; Cavalié et al., 2013). The effect of tropospheric water vapor is also crucial for InSAR time series analysis, with Massonnet et al. (1994), Simons and Rosen (2007), and Hooper et al. (2012) pointing out that substantial improvements in deformation accuracy can be achieved by reducing atmospheric effects before temporal filtering. Thus, to use the vast amounts of newly released InSAR data for more precise deformation monitoring, especially for longer time series and anywhere globally, a generic atmospheric correction model with global coverage, available and useable for all times and in near real time, is required.

One of the approaches used to mitigate tropospheric effects on InSAR measurements has been stacking/filtering, which seeks to capture the spatial-temporal properties of water vapor and attempts to

separate the tropospheric noise from the ground motion signal without any external information (e.g., Ferretti et al., 2001; Fruneau & Sarti, 2000; Hooper et al., 2004; Williams et al., 1998). Although this type of approach is straightforward to apply, the stacking/filtering procedures can mask temporally variable geophysical signals such as creep and slow slip and degrade the temporal resolution of InSAR measurements (Doin et al., 2009). The correlation analysis between interferometric phases and/or topography solves for the topography-correlated or stratified component but ignores the spatial variability of tropospheric signals and can be easily biased by orbit and topographic errors (Béjar-Pizarro et al., 2013; Delacourt et al., 1998; Elliott et al., 2008). Bekaert, Hooper, et al. (2015) dealt with the spatially varying tropospheric signal in the presence of deformation by a power law analysis, but the approach relies on finding a spatial band of topography-correlated atmospheric phase screen not contaminated by other sources such as turbulence, orbit errors, and deformation (Bekaert, Walters, et al., 2015). Moreover, a limitation of the above-mentioned methods is the difficulty in quantifying their performance.

Another more advanced type of tropospheric correction model incorporates external data sets. To date, these have included those from numerical weather models such as the ECMWF Re-Analysis (ERA)-Interim (6-hourly, 0.75° horizontal resolution) from the European Centre for Medium-Range Weather Forecasts (ECMWF; Doin et al., 2009; Jolivet et al., 2011) and the Weather Research and Forecasting model (WRF, e.g., Bekaert, Walters, et al., 2015; Nico et al., 2011); from direct observations such as National Aeronautics and Space Administration's Moderate Resolution Imaging Spectroradiometer (MODIS, e.g., Li et al., 2005; Li, Fielding, Cross, & Preusker, 2009) and European Space Agency's Medium Resolution Imaging Spectrometer (e.g., Li, Muller, et al., 2006; Li et al., 2012), and from tropospheric delays interpolated from those estimated at Global Positioning System (GPS) stations (e.g., Emardson et al., 2003; Li, Fielding, et al., 2006; Onn & Zebker, 2006; Yu et al., 2018). While MODIS provides 1.0- to 1.2-mm root-mean-square (RMS) water vapor agreement with radiosondes and GPS and high spatial resolution maps (Li, Fielding, Cross, & Preusker, 2009), they are restricted to cloud free conditions and are not coincident in time with the recently launched Sentinel-1 and ALOS-2 satellites (typically over 5-hr difference). Weather models such as the ERA-Interim products are often released with a latency of several months and suffer from coarse temporal and/or spatial resolution and failures in accurately capturing atmospheric turbulence (Foster et al., 2013; Jolivet et al., 2011; Webley et al., 2002), with Bekaert, Walters, et al. (2015) reporting a 1.7-cm RMS displacement error of corrected interferograms over Mexico and Italy, after applying corrections generated from ERA-Interim and WRF. The resulting correction map was not sufficient to capture the topography-correlated tropospheric signals and local weather turbulent variations. Conversely, GPS provides continuous estimates (e.g., every 5 min) of water vapor under all-weather conditions and is capable of capturing small features of tropospheric turbulence (e.g., Li, Fielding, et al., 2006; Onn & Zebker, 2006; Williams et al., 1998). Yu et al. (2018) summarize GPS-based correction models to date and demonstrate that subcentimeter RMS displacement and phase standard deviation (StdDev) are possible when using their recent iterative tropospheric decomposition (ITD) model (Yu et al., 2017) and which leads to greater improvements than previous methods. However, such InSAR correction quality is dependent on the availability of sufficiently dense and geometrically sound networks of GPS stations, which are not available everywhere globally. Lofgren et al. (2010) attempted to combine both GPS and ECMWF to generate tropospheric correction maps utilizing both the high spatial resolution of ECMWF and the high accuracy of the GPS. However, they simply used GPS to calibrate ECMWF zenith total tropospheric delays (ZTDs) instead of properly weighting and integrating them, and therefore, their approach may fail if few GPS stations are available or the network exhibits poor geometry.

All of the external tropospheric correction methods discussed above have been used to correct atmospheric effects in InSAR measurements with some degree of success, but they all have their inherent limitations, and it is clear that there is no single method that can be routinely applied at all times, independent of clouds, anywhere globally in near real time for fast event response. In this paper, we seek to address this, by developing a generic InSAR atmospheric correction model that integrates the now global 0.125° × 0.125° horizontal resolution (and improved vertical resolution of 137 levels) 6-hourly High Resolution ECMWF numerical weather model which has a latency of 5–10 hr (termed *HRES-ECMWF*, https://www.ecmwf.int/en/forecasts/datasets/set-i), and the high accuracy, time continuous pointwise ZTD measurements from GPS. We realize this by extending the state-of-the-art ITD model (Yu et al., 2017) to generate tropospheric correction maps from the tight coupling of ZTD observations from both ECMWF and GPS, properly weighted, and investigate the impact of GPS network geometry and regional topography on their combination. The generic correction

model is tested on eight globally distributed Sentinel-1 interferograms, chosen to incorporate flat and mountainous topographies, midlatitude and polar regions, monsoon and oceanic climate systems, and GPS station distributions ranging from none to a spacing of about 12 km. A set of model performance indicators is also provided, to help ascertain the likely success of applying the modeled tropospheric corrections to InSAR measurements, and aid in the development of an automated, near real-time processing chain.

2. Methodology: Integration of GPS and HRES-ECMWF

Tropospheric delay is a common, well-documented error on the measurement of satellite-Earth distance (e.g., Berrada Baby et al., 1988; Hopfield, 1971). The delay is generally caused by the spatial-temporal changes of atmospheric refractivity, which is primarily affected by pressure, temperature, and water vapor content, and has the form (Berrada Baby et al., 1988):

$$\Delta L = 10^{-6} \int_{z_0}^{\infty} N dz = 10^{-6} \left[\frac{k_1 R_d}{g_m} P(z_0) + \int_{z_0}^{\infty} \left(k_2' \frac{e}{T} + k_3 \frac{e}{T^2} \right) dz \right] M_e \tag{1}$$

where ΔL is the tropospheric delay along the satellite-Earth path in meters, N is the refractive index, $P(z_0)$ is the surface pressure in pascals at altitude z_0, g_m is the gravitational acceleration averaged over the troposphere in meter per square second, e is the water vapor pressure in pascals, T is the temperature in kelvin, and M_e is the mapping function that projects the ZTD to slant total delays based on the satellite elevation angle. The remaining terms are constants: $R_d = 287.05$ J kg^{-1} K^{-1}, $k_1 = 0.776$ K Pa^{-1}, $k_2' = 0.233$ K Pa^{-1}, and $k_3 = 3.75 \times 10^3$ K^2 Pa^{-1}.

The interferometric phase $\Delta\varphi$ of geometrical configuration of repeat-pass SAR interferometry can be written as (Zebker et al., 1997)

$$\Delta\varphi = \varphi_1 - \varphi_2 = \frac{4\pi}{\lambda} (\mathbf{r}_1 - \mathbf{r}_2) + \frac{4\pi}{\lambda} \left(\Delta L_1^{LOS} - \Delta L_2^{LOS} \right) \tag{2}$$

where λ is the wavelength of the radar signal, $\mathbf{r_1}$ and $\mathbf{r_2}$ are the slant range vectors corresponding to the first and second acquisitions, respectively, ΔL_1^{LOS} and $\Delta L s_2^{LOS}$ are atmospheric propagation delays of radar signals in the line of sight (LOS).

The features of tropospheric delays acting on an interferogram, which have been studied by numerous researchers (Doin et al., 2009; Lavers et al., 2016; Onn & Zebker, 2006; Williams et al., 1998; Yu et al., 2018), can be generally considered as the sum of (i) a vertically stratified component highly correlated with topography and (ii) a turbulent component resulting from turbulent processes in the troposphere varying both in space and time. The turbulent signals, related to topography-independent spatial changes of temperature, pressure, and water vapor, as well as extreme weather scenarios, can dominate at local scales but are often coupled with the stratified signals which makes it hard to separate them. The long-wavelength tropospheric component could manifest as either topography-related (e.g., in some gently sloping areas) or turbulent, or both. For precise InSAR atmospheric correction, it is important to account for both the stratified and turbulent components.

To model GPS and HRES ECMWF consistently and capitalize on the high spatial resolution of ECMWF and the high quality of GPS-estimated tropospheric delay, we extend the ITD approach developed by Yu et al. (2017) to an integrated model. We use the exponential function to model the stratified delays then construct the turbulent part of the delay by fitting an interpolating scheme based on inverse distance weighting (IDW) to the remaining delays. In the model, the total delays are defined as:

$$ZTD_k = S(h_k) + T(\mathbf{x}_k) + \varepsilon_k \tag{3}$$

where, for the GPS and ECMWF integrated ZTD at location k, T represents the turbulent component and $\mathbf{x}_k$ is the station coordinate vector in the local topocentric coordinate system, S represents the stratified component correlated with height h, and ε represents the remaining unmodeled residual errors, including unmodeled stratified and turbulent signals. The stratified components are modeled as

$$S_i = L_0 e^{-\beta h} => \begin{cases} S_m^G = L_0 e^{-\beta h_m} \\ S_n^E = L_0 e^{-\beta h_n} \end{cases}, P_i = \begin{bmatrix} P_G & 0 \\ 0 & P_E \end{bmatrix} \tag{4}$$

where the modeled stratified delay S is represented by an exponential function with coefficient β, L_0 is the stratified component delay at sea level and h is the height, G represents GPS and E represents HRES-ECMWF. The equation holds within a defined tropospheric decorrelation distance from the point being interpolated. We define this as 150 km, following Emardson and Johansson (1998) and Emardson et al. (2002) who imply that estimating a constant pair of exponential coefficients with this 150-km decorrelation distance will lead to small residuals, which could be handled well by IDW interpolation. Larger decorrelation distances will result in larger residuals which are harder to predict by IDW interpolation, and smaller distances will cause discontinuities in the ZTDs across small pixel areas due to rapidly changing exponential coefficients arising from insufficient GPS stations for their reliable estimation.

We use all ZTD samples in the region considered to estimate the two coefficients β and L_0 in a least squares algorithm. Extra reference locations are needed outside of the interferogram bounds (up to the defined decorrelation distance) to avoid any need to extrapolate rather than interpolate. The ZTDs used (hereafter called reference location ZTDs) include both the GPS ZTD at position m (S_m^G) and the ECMWF ZTD at position n (S_n^E). The weight matrix P_i is defined according to the different quality of GPS and ECMWF ZTDs, and there are three principal factors that influence this: (i) the quality of GPS ZTD is higher than ECMWF ZTD, especially when there are large time differences between ECMWF and InSAR acquisitions (Bock et al., 2005); (ii) GPS ZTD captures the tropospheric temporal variations better than ECMWF ZTD, which is essential in InSAR atmospheric corrections; and (iii) the higher spatial resolution and uniform distribution of ECMWF make it better than GPS for interpolation. A method based on cross validation is proposed in section 3 to automatically determine the relative weights between GPS and ECMWF.

The turbulent part is modeled by a modified IDW to incorporate both ECMWF and GPS ZTDs and reads as

$$T_u = \sum_{i=1}^{k} w_{ui} T(\mathbf{x}_i), \quad w_{ui} = \left. p_i d_{ui}^{-2} \middle/ \sum_{i=1}^{k} p_i d_{ui}^{-2} \right. \tag{5}$$

where u and i are indices for the user and reference locations, respectively. Each turbulent delay at the user location is assigned a weight of w_{ui}, which is determined by the horizontal distance from the user to reference location (d_{ui}) and the weighting (P_i) for GPS and ECMWF, respectively (the same as in the case of the stratified delays as per equation (4)).

The detailed integrated ITD implementation steps are as follows:

1. For each map pixel, the surrounding ZTDs from all reference locations (GPS stations and/or ECMWF nodes) within the decorrelation range limit from the pixel are used to estimate initial values for the exponential coefficients β and L_0, assuming the turbulent components in equation (3) are zero.
2. The residual ε_k on each reference location is computed by subtracting the stratified delay (as modeled at each reference location using the single pair of estimated exponential coefficients) from the ZTD. In the first iteration, the residual contains all of the turbulent component.
3. The turbulent component, T in equation (3), is computed per reference location from the residuals ε_k using IDW interpolation (the weights w_{ui} are computed from equation (5)), as given in equation (6):

$$
\begin{bmatrix} T_1 \\ T_2 \\ \dots \\ T_n \end{bmatrix} =
\begin{bmatrix}
0 & w_{12} & \dots & w_{1n} \\
w_{21} & 0 & \dots & w_{2n} \\
\dots & \dots & 0 & \dots \\
w_{n1} & \dots & w_{n,n-1} & 0
\end{bmatrix}
\begin{bmatrix} \varepsilon_1 \\ \varepsilon_2 \\ \dots \\ \varepsilon_n \end{bmatrix}
\tag{6}
$$

4. The updated values for the turbulent component per reference location are subtracted from the ZTD in equation (3), and a new set of exponential coefficients obtained.
5. Steps (2) to (4) are repeated until the exponential coefficients β and L_0 converge. Yu et al. (2017) show that convergence is typically obtained within about seven iterations.
6. The ZTD for the pixel considered is then obtained by interpolating the turbulent components and residuals from all reference locations and added to the stratified delay computed using the final values of the exponential coefficients for the pixel considered.
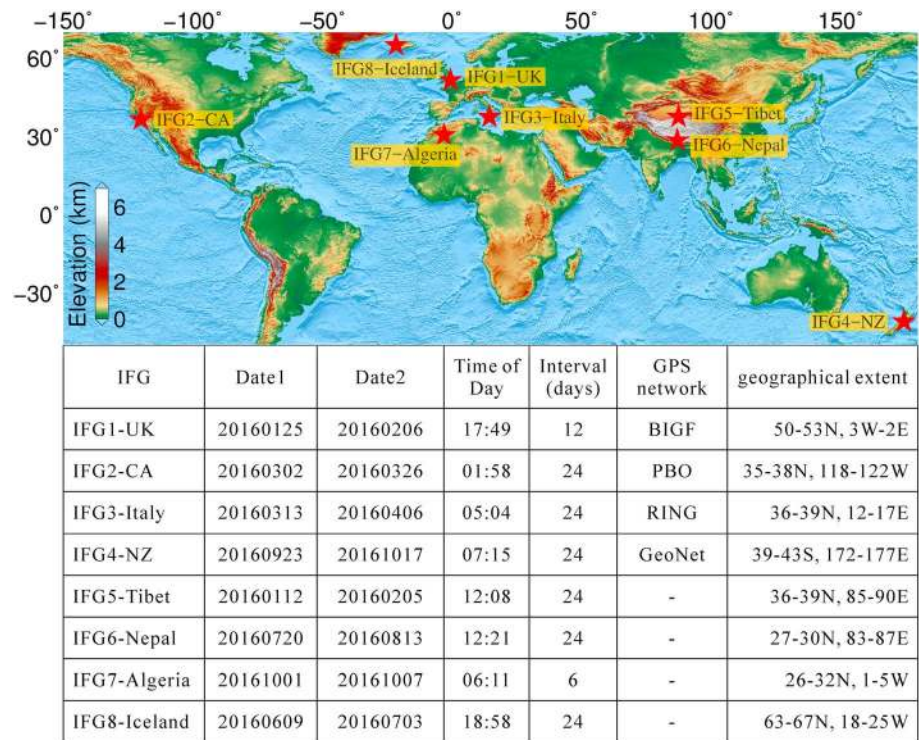
IFG	Date1	Date2	Time of Day	Interval (days)	GPS network	geographical extent
IFG1-UK	20160125	20160206	17:49	12	BIGF	50-53N, 3W-2E
IFG2-CA	20160302	20160326	01:58	24	PBO	35-38N, 118-122W
IFG3-Italy	20160313	20160406	05:04	24	RING	36-39N, 12-17E
IFG4-NZ	20160923	20161017	07:15	24	GeoNet	39-43S, 172-177E
IFG5-Tibet	20160112	20160205	12:08	24	-	36-39N, 85-90E
IFG6-Nepal	20160720	20160813	12:21	24	-	27-30N, 83-87E
IFG7-Algeria	20161001	20161007	06:11	6	-	26-32N, 1-5W
IFG8-Iceland	20160609	20160703	18:58	24	-	63-67N, 18-25W

Figure 1. Sentinel-1 interferograms (denoted as IFG) used in this study. All times are in UTC.

The ITD model is run individually for every pixel across the interferogram, computing a pair of stratified exponential coefficients per pixel. However, as there is usually substantial overlap among the reference locations used for adjacent pixels, the estimated coefficients change only gradually over small scales.

The ITD model uses the ZTDs integrated from the layered temperatures, pressures and the partial water vapor pressures from ECMWF (Jolivet et al., 2011) to enable the decomposition of the stratified and turbulent components in a way consistent with the GPS delays, which is critical to integrate them, and a high computing efficiency. Given the fact that the vertical profile of water vapor over large scales varies exponentially (Ehret et al., 2000; Rocken et al., 1997), ITD seeks a local average vertical profile for each map pixel by its surrounding reference grid nodes and/or reference GPS stations and fit to an exponential function. To avoid overinterpretation, any disturbances on this assumption will drop into the turbulent component, which is iteratively handled in the ITD model. In general, the elevation dependent and medium to long-wavelength tropospheric delays can be well reconstructed by ITD, but the short-wavelength (e.g., a few kilometers) delays require a dense GPS network. While some GPS ZTDs have been assimilated into ECMWF, principally from continuously operating GPS stations in Europe, the integrated ECMWF+GPS ITD approach is still needed because of (i) the coarse temporal resolution (6 hr) of the ECMWF model and (ii) the GPS data assimilated into HRES-ECMWF are used for forecasting, which poses modeled ZTD uncertainties compared to the GPS ZTD estimates themselves.

3. Data Sets and Weighting Strategy

This section describes details of the data sets used for the generation of integrated ECMWF and GPS ZTD correction maps, and the SAR interferograms for the regions considered. The ZTD data were first evaluated by cross validation, from which the relative weights between GPS and ECMWF were determined.

3.1. Data

We selected eight Sentinel-1 Terrain Observation by Progressive Scans interferograms (IFGs) distributed globally (Figure 1). These interferograms represent typical problematic scenarios in InSAR processing such as strong, long-wavelength signals caused by water vapor, large topography variations, large time latency of
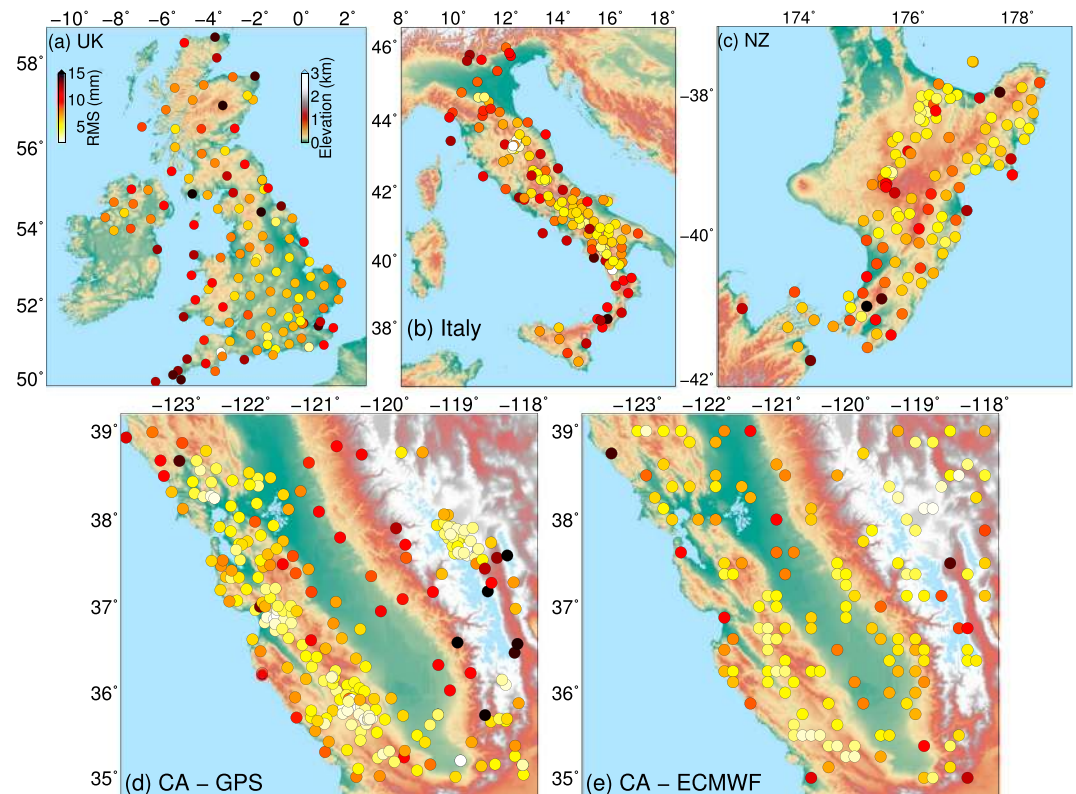
Figure 2. Cross validation: mean RMS differences for each station in the four GPS networks and European Centre for Medium-Range Weather Forecasts (ECMWF) in 2016. Note that the 20% of ECMWF points used were selected randomly from the original 0.125 degree spacing grids.

the ECMWF data, and the effect of the different densities of GPS networks, in that they cover the four GPS networks (described below) to test the benefit of ECMWF combined with GPS but of various station spacings. They also include four areas of geophysical interest where there are no GPS stations, namely, Tibet, Nepal, Algeria, and Iceland, in order to test the global applicability of the generic model but in scenarios whereby only ECMWF can be used. The IFGs were processed with the GAMMA software (http://www.gamma-rs.ch), with the topographic phase contribution removed using a 3 arc sec (~90 m) Shuttle Radar Topography Mission (SRTM) digital elevation model (Farr et al., 2007). For IFG8-Iceland, which is outside the covering range of SRTM, we used the Advanced Space borne Thermal Emission and Reflection Radiometer Global Digital Elevation Model Version 2 instead (Tachikawa et al., 2011). For each interferogram, we generated ZTD maps using the integrated ITD model and projected them to the LOS direction of the InSAR observations with the Global Mapping Function mapping function (Boehm et al., 2006). The HRES-ECMWF data were temporally interpolated to fit the InSAR acquisition times (see section 5.3).

We used four networks of continuously operating GPS reference stations located respectively in Central California (CA), North of New Zealand (NZ), Italy and the United Kingdom (UK), each one characterized by different geometry and station density, ranging from an average spacing of 43 km for the UK network to 12 km for CA (Figure 2 and Table 1). All GPS data for the whole of year 2016 from all stations in the four networks were processed using the PANDA software (Liu & Ge, 2003) in Precise Point Positioning static mode, as described in Yu et al. (2018). Twenty-four hour sessions were used, with JPL *repro2* satellite orbits and 30-s clocks held fixed. The ZTDs were estimated every 5 min as a random walk parameter (a process noise of $5.0E{-}8$ km·s$^{-0.5}$ was applied), together with north-south and east–west tropospheric gradients in a least squares adjustment procedure. We employed the Global Mapping Function mapping function, used the ionospherically-free carrier phase and pseudorange observables, and applied International Global Navigation Satellite System Service models for satellite and receiver antenna phase center variations, along with FES2004 ocean tide loading (coefficients obtained from http://holt.oso.chalmers.se/loading) and Earth

Table 1
Cross Validation for Four GPS Networks and One ECMWF Area Using Daily Values at 14:00 Local Time for All of the Year 2016

Network	Location	Average spacing (km)[a]	Slope	Intercept (m)	Bias (mm)	RMS (mm)	Correlation	Mean RMS (mm)[b]
BIGF[c]	UK	43	0.973	0.065	0.2	9.8	0.97	9.3
RING[d]	Italy	30	0.993	0.015	0.1	8.5	0.99	8.8
GeoNet[e]	New Zealand	17	0.995	0.012	0.2	7.8	0.99	7.7
PBO[f]	California, United States	12	1.000	0.001	0.1	6.6	1.00	6.6
ECMWF[g]	California, United States	12	0.997	0.006	0.0	6.3	1.00	5.9

[a]The spacing is computed as the mean distance between each station and its closest station. [b]The mean daily root-mean-square (RMS) differences for the year 2016. [c]British Isles continuous Global Navigation Satellite System Facility (www.bigf.ac.uk/) at 50–59°N, 11°W–2°E. [d]Rete Integrata Nazionale GPS (ring.gm.ingv.it/) at 37–47°N, 8–18°E. [e]Modern geological hazard monitoring system in New Zealand (www.geonet.org.nz/) at 37–42°S, 173°–179°E. [f]Plate Boundary Observatory (pbo.unavco.org/) at 34°–39°N, 124°–118°W. [g]For European Centre for Medium-Range Weather Forecasts (ECMWF), values were taken at 10:00 or 11:00 local time.

tide displacements (Petit & Luzum, 2010), phase wind up (Beyerle, 2009), relativistic effects, and pseudorange Differential Calibration Delays (Kouba & Héroux, 2001).

We also used output from the model level operational HRES-ECMWF product. Specifically, modeled surface pressure, temperature, and specific humidity were used to calculate ZTDs and precipitable water vapor (PWV) at each 0.125° grid point (i.e., spacing of approximately 9–12 km), as described in Jolivet et al. (2011). While forecast products can potentially introduce pluriannual time series trends when compared with reanalysis products, we expect such effects to be small here as the HRES-ECMWF product is not purely forecasted, but computed using a uniform procedure over time, combining short-range forecast data with real observations to produce the best fit to both (http://cedadocs.ceda.ac.uk/1218/1/ECMWF_user_guide_2001.pdf).

3.2. Cross Validation of ZTDs

It is crucial to validate the ZTD interpolation performance and check the GPS network distributions before generating and applying atmospheric correction maps for InSAR. Therefore, daily PANDA-derived GPS ZTDs at 14:00 local time (the approximate time of day when the troposphere is most active (Gendt et al., 2004; Wang et al., 2005), although this is not an all-encompassing rule and diurnal variations of PWV can differ from location to location) for all of 2016 were cross validated. In this, one point from the whole network of GPS stations was excluded and the ZTD values from the other points used to determine the ZTD at the particular point considered. This procedure was repeated for all stations and the cross-RMS difference computed between the interpolated and original ZTD values. It was also undertaken for ECMWF, but because of the small and regular spacing (and therefore high spatial correlation) of the HRES-ECMWF ZTD data points, this should only be considered as internal cross validation and will always produce a low RMS difference and not realistically reflect the interpolation performance of the whole area. Hence, we randomly chose 20% of points among the regular 0.125° spacing grids to reduce the spatial correlation and then conducted the (internal) cross validation in the same way as for GPS.

The cross-validation RMS differences for all the GPS networks and, for the case of CA, also internal cross validation of HRES-ECMWF, for the year 2016, are summarized in Table 1. We fitted a linear model (actual ZTDs = Slope Interpolated ZTDs + Intercept) for each network including HRES-ECMWF. We used the local time 14:00 for all GPS networks, but for ECMWF over CA, we used 18:00 UTC (local time 11:00 during summer and 10:00 during winter) to avoid ECMWF temporal interpolation. The average GPS station spacing decreases from the UK, Italy, NZ, to CA networks, and their corresponding RMS reduce accordingly: the UK network exhibits the greatest average station spacing (43 km), which leads to an RMS of 9.8 mm compared with 6.6 mm for the 12-km spacing CA network. The HRES-ECMWF of CA has a similar spacing to the CA GPS network but a slightly lower RMS, which is attributed to the GPS ZTD capturing more detailed turbulent signals and thus degrading the interpolation performance. The RMS differences per station are plotted in Figure 2, which shows that more precise interpolated ZTDs are generated in areas with a denser GPS network. Larger RMSs mostly arise in areas with fewer stations or on the edge of the networks. However, all regions present a mean correlation coefficient using all stations of at least 0.97 and a bias varying between 0 and 0.2 mm. A summary of multiple statistical metrics that were computed is given in Table 1.
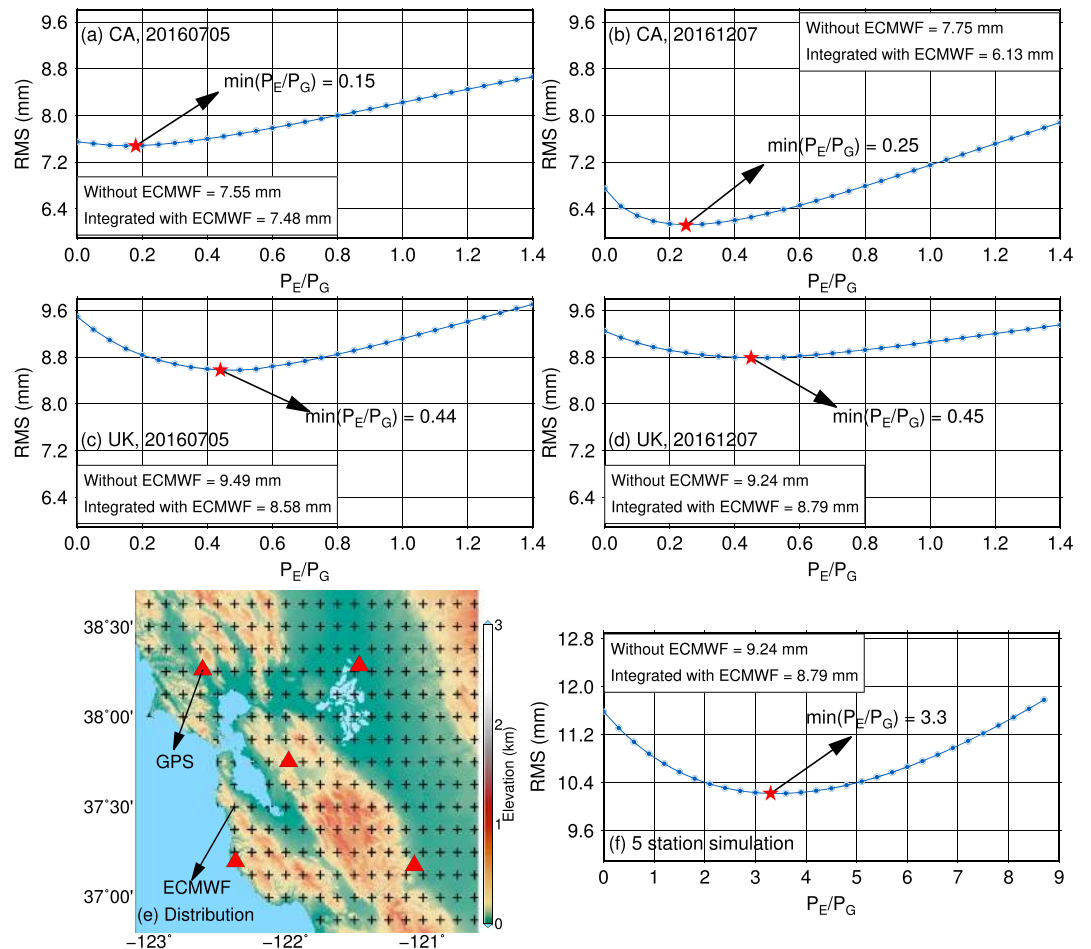
Figure 3. Relative weighting between GPS and European Centre for Medium-Range Weather Forecasts (ECMWF) zenith total tropospheric delays on integrating, using the Central California (CA; (a) is 20160705 and (b) is 20161207) and UK GPS networks (c is 20160705 and d is 20161207). The y-axes represent the cross-root-mean-square (RMS) for all GPS stations on the dates shown. Station distributions are given in Figure 2. The horizontal axes represent the relative weighting between HRES-ECMWF (P_E) and GPS (P_G). (e) is a simulated network with five stations in CA and (f) is its corresponding optimal relative weight determination.

3.3. Weight Determination

After independently validating the qualities of the interpolated GPS and ECMWF ZTDs, they should be properly weighted in the integrated ITD model. Since the cross validation reflects the ZTD interpolation performance and the GPS network distributions, we utilized the cross-validation RMS of the GPS network stations to determine the relative weights between GPS and ECMWF.

For a given GPS network, we calculated its cross-validation RMS, but instead of using GPS ZTDs only, we also used the surrounding ECMWF grid nodes to predict ZTDs at each GPS station. This was done by the integrated ITD model described in section 2 and using different ECMWF:GPS relative weights ranging from 0.0 to 10 (at a step of 0.1). The optimum ECMWF:GPS weighting for the particular network was considered that which led to the lowest cross RMS. Figure 3 shows examples using data from the CA (~12-km GPS station spacing) and UK (~43-km GPS station spacing) networks using one day in winter (7 December 2016) and one in summer (5 July 2016). Clear RMS minima can be seen for all cases, arising when applying ECMWF:GPS relative weights of 0.1–0.3 for the denser CA network and 0.4–0.5 for the sparser UK network. A simulation test was also undertaken to show the impact of a network of GPS stations, which has a very sparse distribution. We selected five stations from the CA network on 12:00 UTC 1 January 2016 (Figure 3e) and repeated the cross-validation analysis. The best relative weight was found to be 3.3, which means that in this simulation case, the correction maps should be mainly dictated by ECMWF due to the sparse GPS station distribution.

From the weight determination procedures described above, when the GPS network is sparse, the cross-validation RMS will be higher because of missing short-wavelength components. The ECMWF:GPS relative weighting will depend on how well the ECMWF ZTDs represent the missing signals from GPS (reflected by the integrated ITD cross-validation RMS for the GPS stations). If the ECMWF ZTDs have large time latency (resulting in the ECMWF ZTDs differing significantly from the GPS values), it will not help to improve the cross validation and hence they will be assigned low weight.

The relative weight from cross validation is a spatial-temporally dependent variable that can be easily determined whenever both GPS and HRES-ECMWF data are available and is essential for automated processing. For the four IFGs used here covered by GPS stations, the relative weights were computed as just described, using all GPS data from stations covered by the IFG and also up to 150 km outside its boundaries. For the relevant dates, ECMWF:GPS relative weights of 0.48, 0.22, 1.10, and 1.35 for IFG1-UK, IFG2-CA, IFG3-Italy, and IFG4-NZ were obtained, respectively. Hence, the relative weighting reflects not only the ZTD precision but also the density of the observations, the variation of the topography, and the local tropospheric conditions.

4. Model Evaluations

Having cross validated the interpolated ZTDs and determined the relative weights to be used for the integration of the HRES-ECMWF and GPS ZTDs, ZTD maps were generated and applied to InSAR measurements to correct for atmospheric effects. We first illustrate in Figure 4 the contribution of the stratified and turbulent ZTD corrections by showing the respective maps for an example interferogram (IFG1-UK), computed using the integrated ITD model with both GPS and ECMWF ZTDs input. Maps of their stratified and turbulent components summation and the raw and corrected (by subtracting the tropospheric delays from the summed stratified and turbulent components) interferograms are also shown. They illustrate that most of the tropospheric errors on IFG1 are represented as long wavelength turbulent signals (see Figures 4b and 4d), which are well captured by the ITD model.

We next assessed the performance of the developed integrated ITD model by using it to correct atmospheric effects on the eight globally distributed interferograms (Figure 1), thus testing its suitability in different parts of the world and when there is a range of GPS ZTDs available, from none through to 12 km station spacing. For the four interferograms, which are covered by GPS networks, we assess and quantify the model's performance when the applied correction is based on GPS ZTDs only, on ECMWF ZTDs only, and from integrated GPS and ECWMF ZTDs. Then, four additional interferograms covering areas without a GPS network are evaluated using ECMWF ZTDs only, to emphasize the global applicability of the model developed. The same decorrelation limit was used per pixel as per the cross validation tests by using only the ECWMF and GPS ZTDs within 150 km of the pixel considered.

Two metrics were used to assess the model's performance, depending on the availability of GPS stations across the interferogram. First, for all interferograms, the LOS range change StdDev across the entire interferogram (250 by 250 km) was computed to assess the uncertainty induced by longer wavelength atmospheric signals, which assumed there was no ground movement between the two image acquisitions (6–24 days), although a large StdDev could also result from actual ground movements such as interseismic motion, postseismic motion, or subsidence due to groundwater extraction (Fruneau & Sarti, 2000; Short et al., 2014). Note that atmospheric errors can also manifest as a ramp in the range direction and the StdDev would not represent its maximum value. The second metric used, for interferograms whose coverage encompassed GPS stations, was the displacement quality by comparing the InSAR displacements at each GPS station with independent 3-D GPS-derived displacements provided by the Nevada Geodetic Laboratory at the University of Nevada, Reno, computed from model fits to the time series of daily GPS coordinate estimates. The GPS velocities were estimated using the MIDAS algorithm (Blewitt et al., 2016), while the other parameters (intercept, annual, and semiannual oscillations) were estimated using least squares. Both InSAR and GPS-derived displacements were converted to LOS, differenced for all GPS stations in the interferogram, and the RMS displacement difference computed.

4.1. Atmospheric Correction With Integrated HRES-ECMWF and GPS

Figure 5 shows the results for IFG1-UK and IFG2-CA, which represent different station spacings. It appears that both raw interferograms exhibit strong atmospheric effects, with raw phase StdDev values of 2.75 and
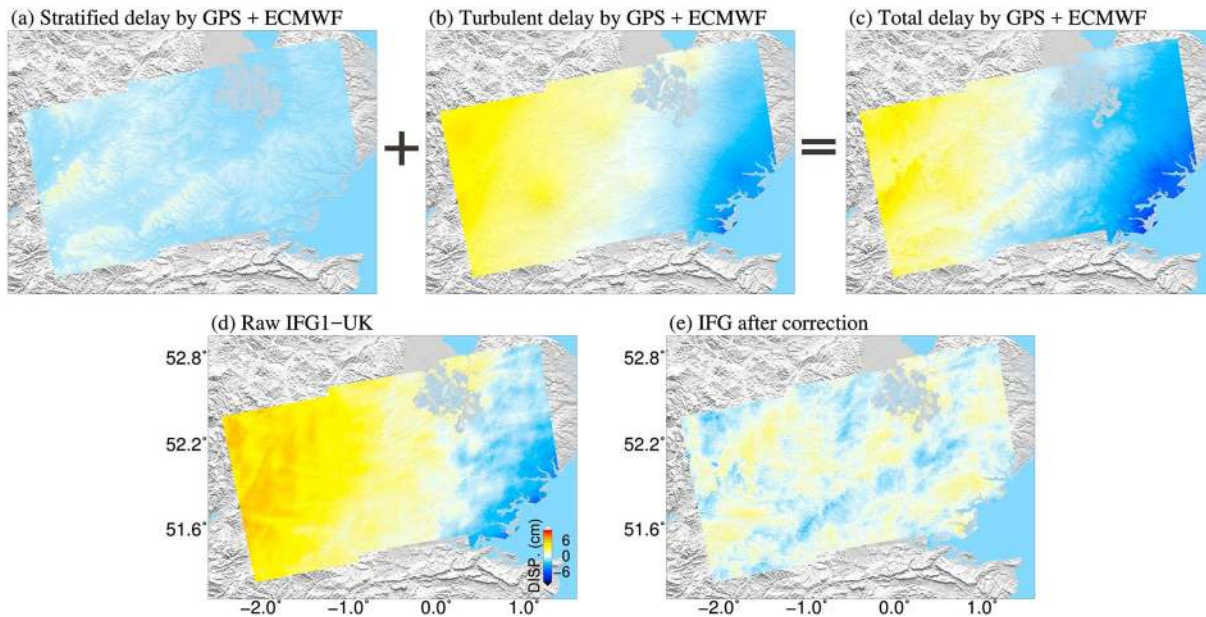
Figure 4. Modeled tropospheric stratified (a) and turbulent (b) zenith total tropospheric delay components for the IFG1-UK interferogram when using integrated GPS and European Centre for Medium-Range Weather Forecasts (ECMWF). (c) is the total delay map. Also shown are the raw (d) and corrected (e) interferograms. The phase standard deviation and displacement root-mean-square improvement statistics are given in Figure 5a.

2.44 cm, respectively. The long-wavelength atmospheric effect on IFG1-UK disappeared and the phase StdDev dropped to 0.71 cm after applying the GPS-only atmospheric correction map, to 1.02 cm after ECMWF correction and to 0.69 cm after the integrated correction, as listed in Table 2. The displacement RMS differences compared with GPS also decreased dramatically after correction, particularly for the integrated correction, which shows a 71% improvement of 2.23 to 0.65 cm. It can be seen from Figure 5 that the remaining signals are mostly short wavelength and topography correlated, especially after applying the ECMWF correction, indicating that these remaining signals, or at least parts of them, are unmodeled atmospheric delays. Elliott et al. (2008) used a linear fit with height to reduce such effects, but the method fails when the deformation signals are correlated with topography or the relationship between phase and height is not constant throughout the interferogram.

Similar improvements are also observed in Figure 5 for IFG2-CA, with 54% improvement in terms of phase StdDev after GPS correction, 41% after ECMWF correction and 61% after the integrated correction, reducing from 2.44 cm to 0.96 cm. The displacement measurements compared with GPS improved by 70% after the integrated correction, with most of the errors per GPS station falling to below 1 cm as can be seen in Figure 5b, and an RMS displacement error of 0.72 cm. Although the IFG2-CA GPS network is denser than that for IFG1-UK, it is unevenly distributed, resulting in most of the improvements after applying GPS corrections occurring in the west (Figure 5b2) where most of the GPS stations are located, whereas improvements on the eastern part of the interferogram are limited. The large topography variation in this area makes it harder to model the atmospheric delays compared with the flatter terrain in the UK, and the lower performance of ECMWF (41% StdDev improvement) compared with IFG1-UK (63% StdDev improvement) reflects this (topography effects are further considered in section 5.4). Hence, the different performances of GPS for the two interferograms indicate the dependence on both topography and network geometry.

IFG3-Italy covers most of the island of Sicily and only incorporates a limited number of GPS stations (11, with average spacing 75 km). Figure 6 shows that interferogram atmospheric contamination arises on the west and north coasts, where the raw observations imply substantial ground subsidence but which is not the case in reality. Applying ECMWF corrections results in a 41% StdDev improvement, compared with 36% for GPS (Table 2), with the greater improvement visually apparent in the north-east and south-east of Sicily. The sparse distribution of GPS stations was unable to adequately capture the atmospheric delays around Mount Etna, and the greater improvement (where GPS has performed similarly to ECMWF) is found in the west due to its flat topography. As for IFG1-UK and IFG2-CA, the benefit of applying integrated correction
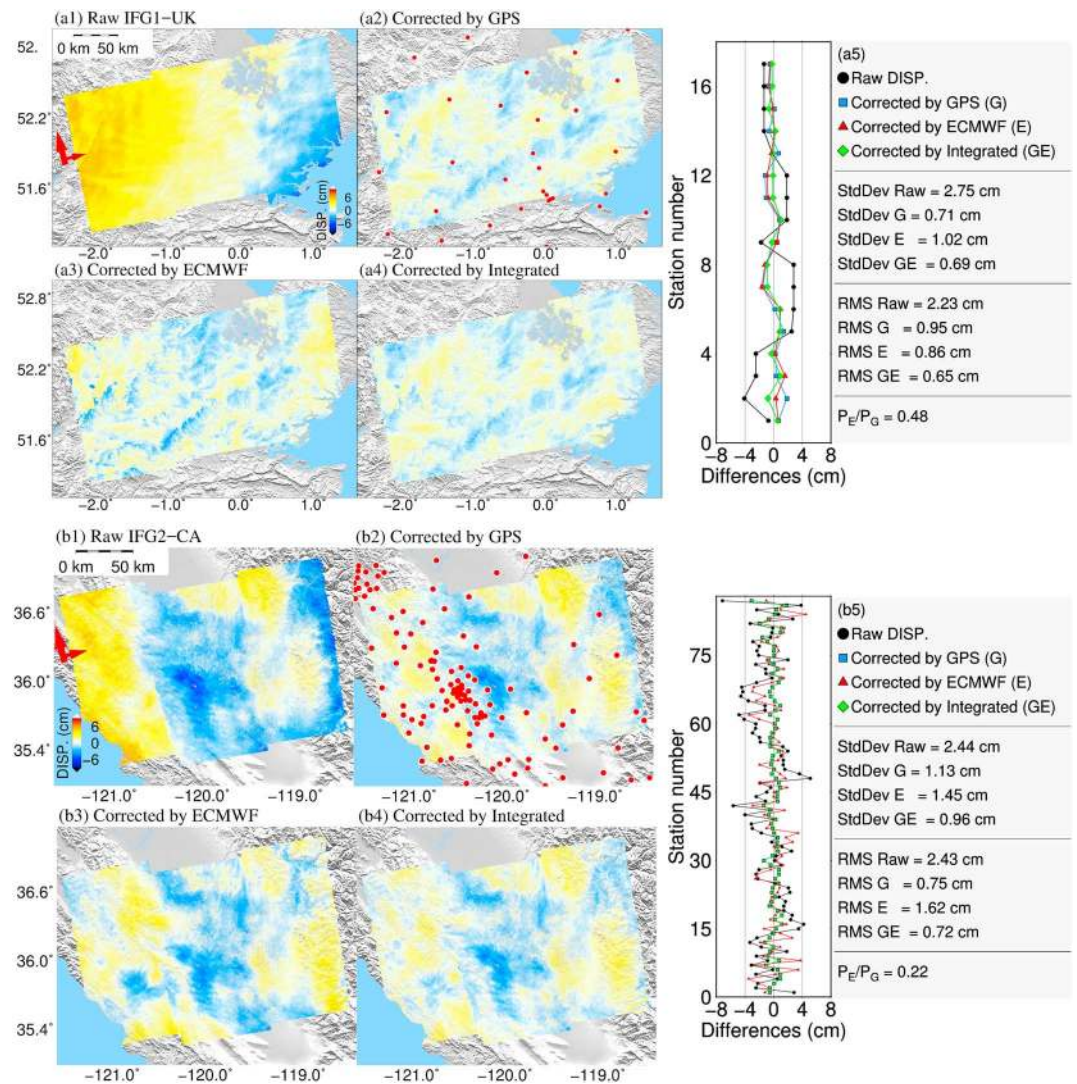
Figure 5. Interferometric synthetic aperture radar atmospheric corrections using GPS (G), European Centre for Medium-Range Weather Forecasts (ECMWF; E), and their combinations (GE) for IFG1-UK (a1–a5) and IFG2-CA (b1–b5). (a1) and (b1) are raw interferograms, (a2) and (b2) are GPS-corrected interferograms, (a3) and (b3) are ECMWF-corrected interferograms, (a4) and (b4) are GPS + ECMWF-corrected interferograms. (a5) and (b5) show the displacement differences between GPS and InSAR per GPS station. Phase standard deviation (StdDev), displacement RMS, and automatically determined ECMWF:GPS relative weight (P_E/P_G) for each IFG are also listed. The red arrows indicate the radar flight direction, and the red circles represent GPS stations. All phases are in line of sight direction.

maps can be seen from Figure 6, with StdDev reductions of 43% obtained (from 1.49 cm to 0.85 cm) and 66% RMS displacement reductions (from 1.37 to 0.47 cm).

The atmospheric correction results for IFG4-NZ shown in Figure 6 follow a similar trend to those for IFG3-Italy: ECMWF resulting in a lower phase StdDev and similar RMS displacement than GPS, with ECMWF removing atmospheric effects in the west where GPS correction is less successful because the GPS station distribution is sparse. Whereas in the east, where the GPS station distribution is much denser (15-km spacing), the GPS corrections perform similarly to ECMWF. As for IFG1-UK, IFG2-CA, and IFG3-Italy, the integrated correction maps result in the lowest phase StdDev (1.10 cm) and displacement RMS (1.12 cm), equating to respective improvements over the raw interferogram of 44% and 44%, respectively.

To summarize, both the GPS and ECMWF atmospheric correction maps are able to substantially improve raw InSAR measurements: for the four interferograms considered, phase StdDev improvements of up to 74% arise on applying GPS corrections and 63% for ECMWF. When a dense GPS network is available, the GPS maps

Table 2
InSAR Atmospheric Correction Performance Statistics Expressed in Terms of Phase Standard Deviation (StdDev) and Displacement RMS for Different Correction Methods Applied on Eight Interferograms

IFG	Phase StdDev				Displacement RMS			
	Raw IFG	GPS correction	ECMWF correction	Integrated correction	Raw IFG	GPS correction	ECMWF correction	Integrated correction
IFG1-UK	2.75	0.71 (74%)	1.02 (63%)	0.69 (75%)	2.23	0.95 (57%)	0.86 (61%)	0.65 (71%)
IFG2-CA	2.44	1.13 (54%)	1.45 (41%)	0.96 (61%)	2.43	0.75 (69%)	1.62 (33%)	0.72 (70%)
IFG3-Italy	1.49	0.95 (36%)	0.88 (41%)	0.85 (43%)	1.37	0.70 (49%)	0.61 (55%)	0.47 (66%)
IFG4-NZ	1.97	1.35 (31%)	1.13 (43%)	1.10 (44%)	1.99	1.23 (38%)	1.30 (35%)	1.12 (44%)
IFG5-Tibet	1.15	—	0.45 (61%)	—	—	—	—	—
IFG6-Nepal	1.83	—	1.11 (39%)	—	—	—	—	—
IFG7-Algeria	2.40	—	0.88 (63%)	—	—	—	—	—
IFG8-Iceland	1.76	—	1.05 (40%)	—	—	—	—	—
Mean	1.97	1.04 (47%)	1.00 (49%)	0.90 (54%)	2.01	0.91 (55%)	1.10 (45%)	0.74 (63%)

Note. Unit: cm. Percentage improvements over the raw measurements are given in parentheses. ECMWF = European Centre for Medium-Range Weather Forecasts; RMS = root-mean-square.

provide more precise corrections and capture the small magnitude, turbulent atmospheric delays better than ECMWF and thus perform better. However, the performance is highly dependent on the station density and distribution (network geometry), as well as the topography, with the GPS corrections when using a sparse network (e.g., IFG3-Italy in Figure 6a2) performing worse than ECMWF. In all four cases considered, the integration of GPS and ECMWF results in the lowest phase StdDev and RMS displacement values.

4.2. Global Applicability of ECMWF-Based Correction Maps

To evaluate the global applicability and performance of the model developed, we applied ECMWF atmospheric corrections to the four interferograms that do not contain any GPS stations, namely, IFG5-Tibet, IFG6-Nepal, IFG7-Algeria, and IFG8-Iceland. The results are shown in Figure 7, displaying the raw and ECMWF-corrected interferograms, and the phase StdDev values are listed in Table 2. It is clear that for the mountainous regions (IGF5-Tibet and IFG6-Nepal), the phase errors are mostly topography correlated and have been corrected by 61% to 0.45 cm StdDev and by 39% to 1.11 cm, respectively. The atmospheric errors on IFG5-Tibet tend to be long wavelength and thus are easier to be captured by ECMWF. The shorter-wavelength effects on IFG6-Nepal, mainly due to the high topography variations, cannot be fully removed using the ECMWF model, and the remaining uncorrected errors are likely to be turbulent signals. It should be noted that for a high-altitude region (which means lower water vapor content on average), a strong turbulence effect can also be observed on interferograms (as here for IFG6-Nepal).

IFG7-Algeria is located in a desert region with fairly low altitude and limited topography variations (altitude 0.8–1.0 km across the IFG). As shown in Figure 7, the magnitude of the atmospheric errors reaches up to ~8 cm (raw phase StdDev of 2.40 cm) but they appear to be mostly associated with a long wavelength signal. After applying ECMWF atmospheric corrections, turbulence errors persist but the phase StdDev has reduced by 63% to 0.88 cm. Conversely, IFG8-Iceland exhibits large topography variations (from 0 to 1.5 km) and is located close to a polar region, where the water vapor content is lower. It can be seen from Figure 7 that the large magnitude (8 cm) atmospheric errors systematically affect the computed displacement across almost the entire interferogram. After correction, the StdDev of the phase errors drops to 1.05 cm (40% improvement) and is partly associated with an elevation dependent signal (the western part where the topography variations are high) and partly with a turbulent behavior (eastern part). Hence, as for IFG5-Tibet and IFG6-Nepal, the HRES-ECMWF based correction model is suitable for obtaining corrected interferograms with a StdDev of ~1 cm or lower.

5. Performance Indicator Metrics

The generic atmospheric correction model developed has been evaluated at different locations globally, encompassing a range of topography, climate and GPS station distributions. The model's performance has been evaluated by considering the phase StdDev and also, for areas including GPS stations, the RMS displacement difference between GPS and InSAR. However, in practice, when actual surface movements occur and there are insufficient GPS stations to cover the whole area, these performance indicators will fail. It is
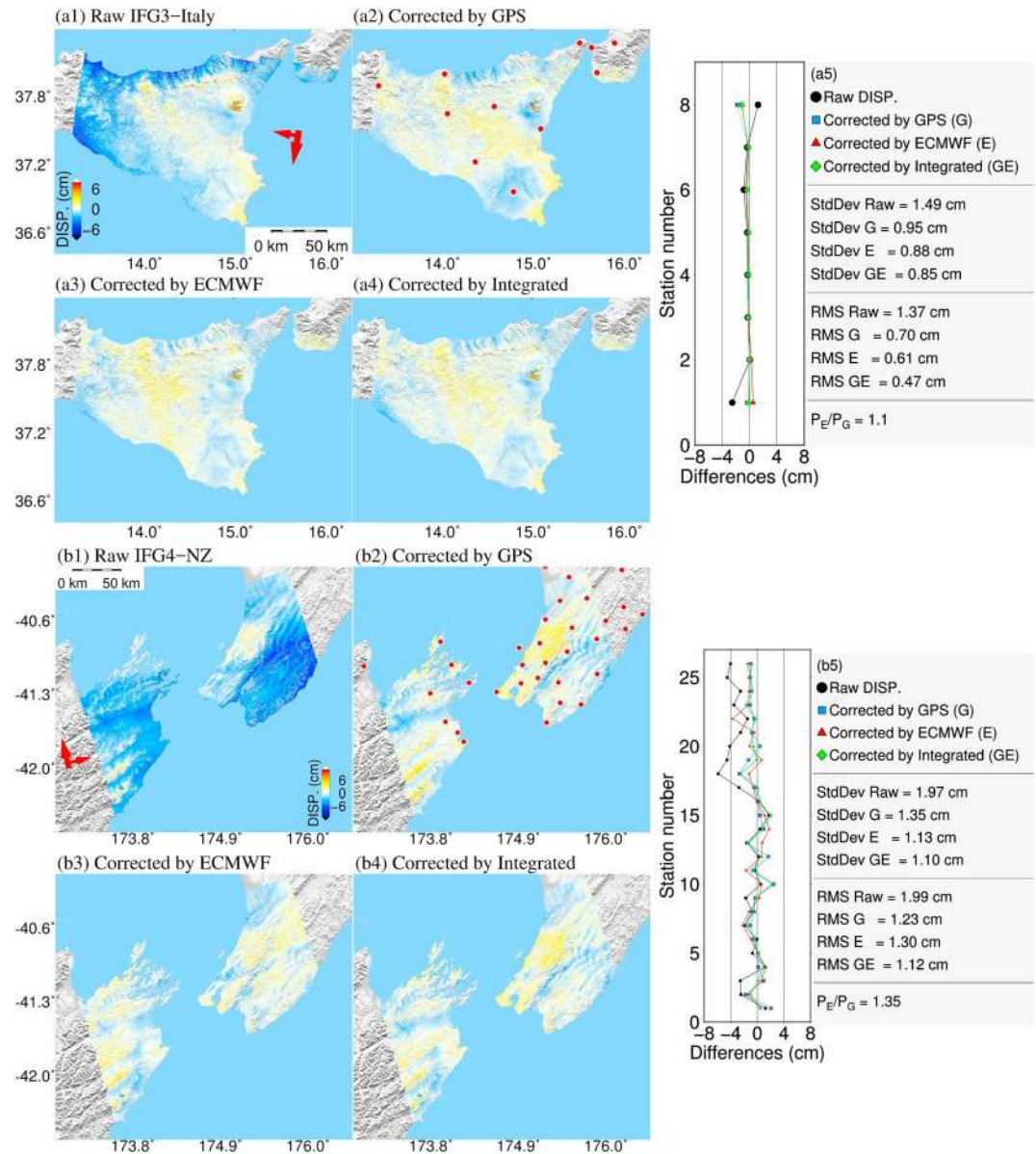
Figure 6. Interferometric synthetic aperture radar atmospheric corrections using GPS (G), European Centre for Medium-Range Weather Forecasts (ECMWF; E), and their combinations (GE) for IFG3-Italy (a1–a5) and IFG4-NZ (b1–b5). Panel descriptions as for Figure 4. The red arrows indicate the radar flight direction, and the red circles represent GPS stations. All phases are in line of sight direction.

therefore important to develop additional performance indicators to inform users of model applicability, including flagging any instances when the modeled atmospheric corrections should not be applied. In this section, we introduce several additional indicators for model interpolation and atmospheric error correction performance, which include (i) cross validation RMS of GPS and HRES-ECMWF ZTD, (ii) correlation analysis between InSAR phase and tropospheric delays, (iii) the time differences between ECMWF and InSAR acquisitions, and (iv) topography variations.

5.1. Indicator 1: ZTD Cross Validation RMS

In section 3, we have used the cross test to validate the interpolation performance of GPS and HRES-ECMWF ZTDs. The RMS of the cross validation reflects not only the pointwise ZTD interpolation precision but also the network geometry, especially for GPS where a nonuniform and sparse station distribution often arises. It was
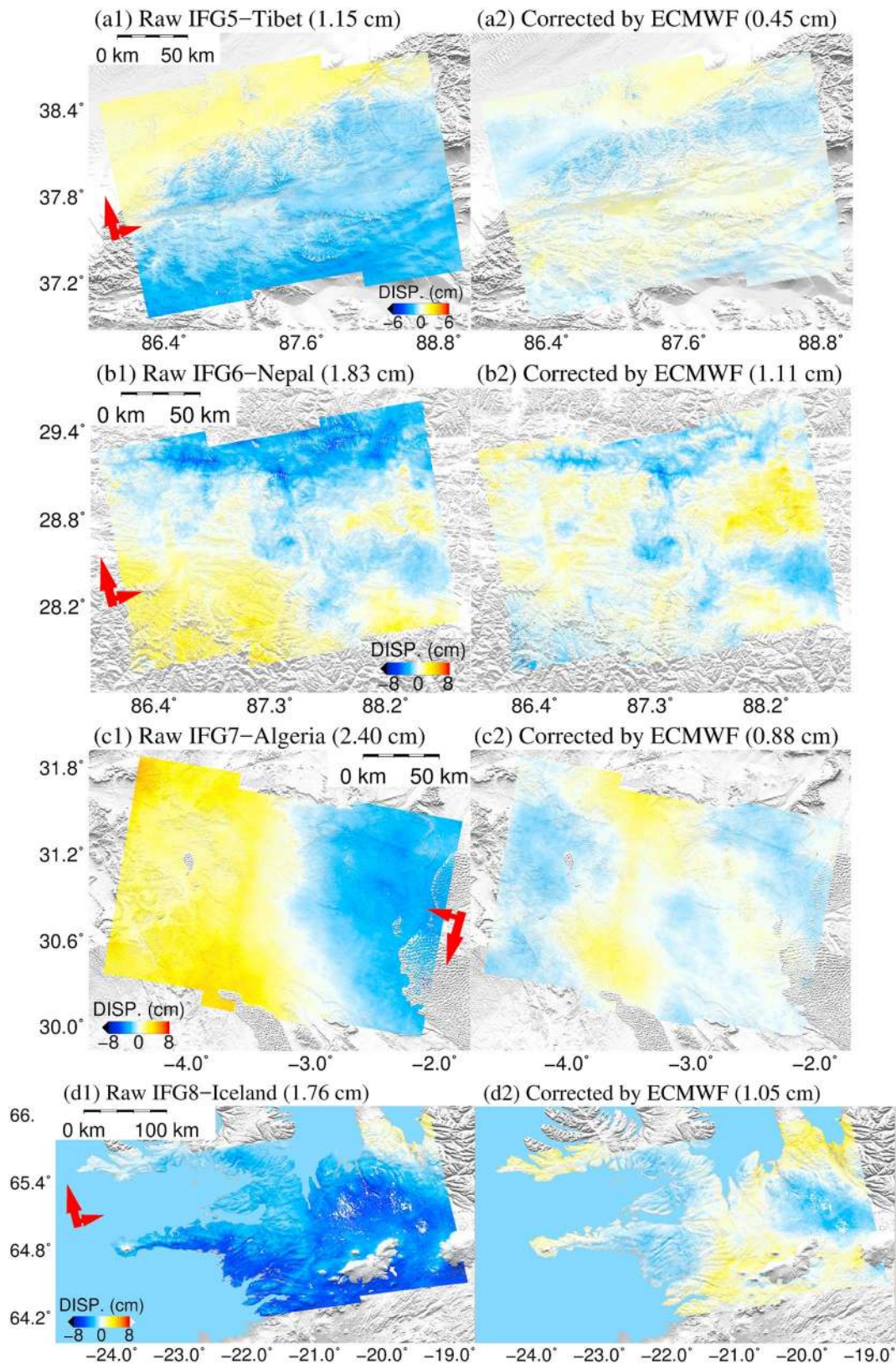
Figure 7. Interferometric synthetic aperture radar atmospheric correction using European Centre for Medium-Range Weather Forecasts (ECMWF) for IFG5-Tibet, IFG6-Nepal, IFG7-Algeria, and IFG8-Iceland. The first and second columns represent the raw and corrected interferograms, respectively. The numbers in parentheses indicate the phase standard deviation before and after correction. The red arrow represents the radar flight direction. All phases are in line of sight direction.

shown in section 4 that GPS corrections perform better than ECMWF for the IFG2-CA dense network case, whereas for the IFG3-Italy and IFG4-NZ cases which have sparser GPS station coverage, the ECMWF corrections perform slightly better than the GPS. One exception is for IFG1-UK where there is a sparse GPS network but the GPS-based corrections perform well. This is mainly due to its flat topography which is another indicator to be discussed later. Section 3.2 also showed that a dense GPS network yields a lower cross validation RMS and vice versa. These results imply that the ZTD cross-RMS may be used as an indicator to reflect the atmospheric correction performance and that a lower ZTD cross-RMS indicates a better station distribution and more precise atmospheric interpolation map. As a result, the cross-RMS of the GPS and HRES-ECMWF ZTDs are calculated, in the same way as in section 3, for each interferogram before utilizing the corrections (Table 3).

5.2. Indicator 2: Phase Versus Estimated Atmospheric Delay Correlation

A high correlation between phase measurements and the computed atmospheric corrections suggests that the model is able to capture most of the atmospheric effects, and thus successful InSAR atmospheric error correction is expected. For all eight interferograms, the correlations between the phase and tropospheric delays (using the integrated model for IFG1–IFG4 and ECMWF for IFG5–IFG8) per pixel are shown in Figure 8, with the statistics per interferogram also listed in Table 3. A high correlation of 0.86 was observed for IFG1-UK, which corresponds to a 75% improvement in terms of phase standard deviaiition reduction (Table 2), whereas for IFG5-Tibet a lower 0.57 correlation, corresponding to a 61% improvement, was obtained. The lower correlation for IFG5-Tibet may be due to the smaller magnitude of the raw phase measurements (StdDev= 1.15 cm compared with 2.75 cm for IFG1-UK before correction) and therefore the atmospheric errors may not be dominating in magnitude.

5.3. Indicator 3: ECMWF Time Difference

The GPS ZTDs are coincident in time with the SAR image acquisitions, but the ECMWF ZTDs are only available every 6 hr, which can lead to time differences between the InSAR measurements and the ECMWF-based atmospheric correction maps. The temporal variation of ZTDs, especially the part due to water vapor during a short time interval (e.g., 2–3 hr) can be substantial and unpredictable and thus may cause the correction to perform poorly (e.g., Li, Fielding, & Cross, 2009; Li, Muller, et al., 2006). To investigate the impact of ECMWF and InSAR acquisition time differences, we used continuous GPS ZTD time series (5-min interval) to evaluate errors of temporally interpolating the 6-hourly ECMWF ZTDs to the measurement epoch. We used the Central California region covered by IFG2-CA, and the GPS data were processed using the same settings as in section 3.1. For each hour of an individual day, we linearly interpolated the nearest 6-hourly ECMWF ZTD values on to all GPS stations and computed the differences against the GPS ZTDs directly estimated at the station and for the hour considered (this approach will hereafter be called *nearest*). This procedure was then repeated for all days of 2016, and the mean RMS difference per hour was averaged for each hour of day (0, 1, 2, …, 23) over the year. These mean hourly RMS values for the year are shown in Figure 9, together with variations (1-sigma), and it can be clearly seen that as the time difference from the ECMWF 6-hourly ZTD times (the model is available at 0, 6, 12 and 18 hr UTC) increases so does the RMS and the 1-sigma range. The RMSs at hours corresponding to the greatest temporal interpolation have a peak value that is nearly 150% of the RMSs at no time difference: approximately 20 mm compared with 12 mm.

To minimize the impact of the time differences, we applied a linear temporal interpolation in our correction model using the two closest ECMWF ZTD samples. It can be seen from Figure 9 that this procedure improves the performance and reduces the peak values from 15 to 10 mm; however, there are still uncertainties during large time difference periods. As a result, we may use time difference as an indicator to highlight potential uncertainty induced by rapidly changing atmospheric conditions.

5.4. Indicator 4: Topography Variations

The ZTD variations and the interpolation performance will all be affected by the topography. To assess this effect, we introduced MODIS Near-Infrared PWV data as *truth* and interpolated the ECMWF PWV (with the same 0.125° grid distribution throughout the region) on to the MODIS PWV grid. Since MODIS PWV has a higher spatial resolution than ECMWF (~1 km compared with ~9–12 km), it can be used to evaluate the ECMWF-based model's interpolation performance relative to local topography variations. As a test case, we selected the region of Central California since it displays considerable topography variations with high

Table 3
Model Performance Indicator Metrics for All Interferograms

IFG	ZTD cross validation linear fit (cm)	ρ[a]	Cross RMS of GPS ZTDs (mm)	Cross RMS of ECMWF ZTDs (mm)	IFG-ECMWF time difference (minutes)	Topography variation
IFG1-UK	$Y = 1.096X - 0.928$	0.86	11.5	8.3	11	Low
IFG2-CA	$Y = 0.699X - 0.952$	0.79	13.1	9.2	118	High
IFG3-Italy	$Y = 0.624X + 0.217$	0.65	12.6	4.8	56	Medium
IFG4-NZ	$Y = 0.693X + 1.014$	0.63	12.0	6.4	75	Medium
IFG5-Tibet	$Y = 0.454X + 0.531$	0.57	—	1.9	8	High
IFG6-Nepal	$Y = 0.669X + 0.522$	0.61	—	7.9	21	High
IFG7-Algeria	$Y = 0.690X + 1.078$	0.66	—	5.1	11	Low
IFG8-Iceland	$Y = 0.718X + 0.112$	0.60	—	4.8	58	Medium

[a]Phase delay correlation. ZTD = zenith total tropospheric delay; ECMWF = European Centre for Medium-Range Weather Forecasts; RMS = root-mean-square.

mountains (~3,500-m altitude) on the west coast and on the eastern portion of the domain, and nearly flat areas in the middle (under 200-m altitude).

We processed all cloud-free MODIS PWV data during 17:50–18:10 UTC (i.e. around 10 a.m. or 11 a.m. local time) on each day of 2016, which coincides with the ECMWF 18:00 UTC model output and hence minimizes any time interpolation errors. The elevation of each MODIS PWV grid was bilinearly interpolated to a uniform grid using the 3 arc sec SRTM digital elevation model. The ECMWF PWV was then interpolated on to the MODIS PWV grid using the ITD model, and the ECMWF PWV agreed with the MODIS PWV with an RMS difference of 1.88 mm (Figure 10e). Figures 10a–10c show the PWV differences for three dates, from which greater differences between observations and ECMWF-derived PWV can be observed in regions with higher PWV contents. This is consistent with the magnitude of errors in other PWV sensors being proportional to the water vapor content, for example, as found for GPS by Glowacki et al. (2006) and for MODIS by Li et al.
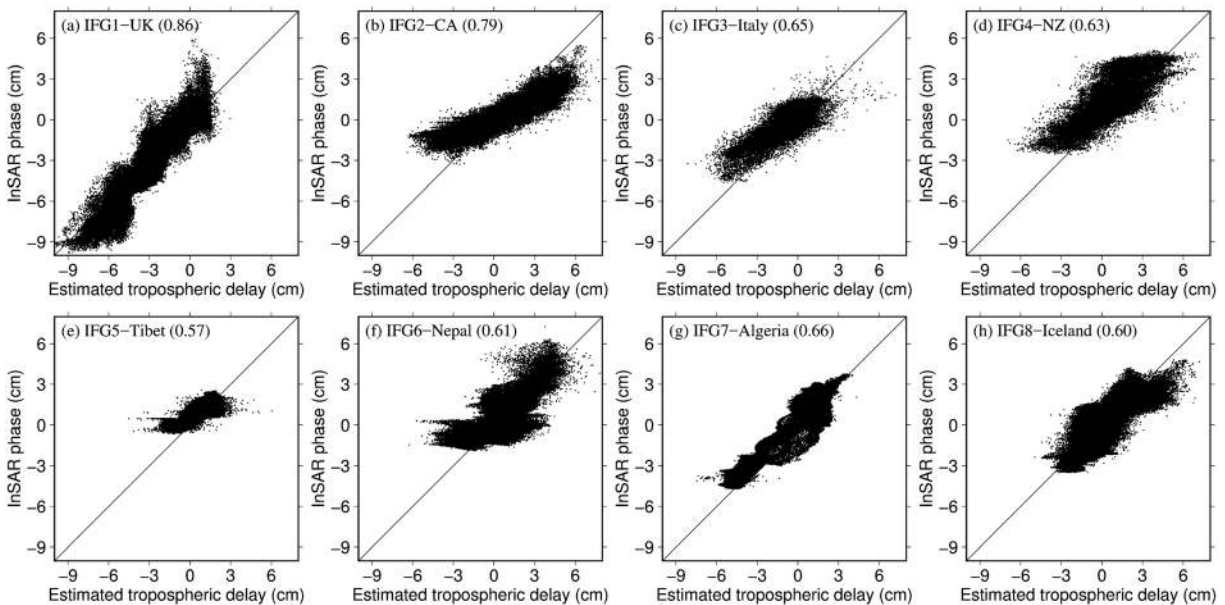

Figure 8. Phase and interpolated tropospheric delay correlations for all pixels in the eight interferograms. The linear relationship between phase and estimated tropospheric delay is phase = slope×delay+intercept. Phase has been converted to raw displacement in cm. Tropospheric delays have been computed using the European Centre for Medium-Range Weather Forecasts and GPS integrated model for IFG1–IFG4, and ECMWF only for IFG5–IFG8. Correlation coefficients are listed in parentheses. InSAR = interferometric synthetic aperture radar.
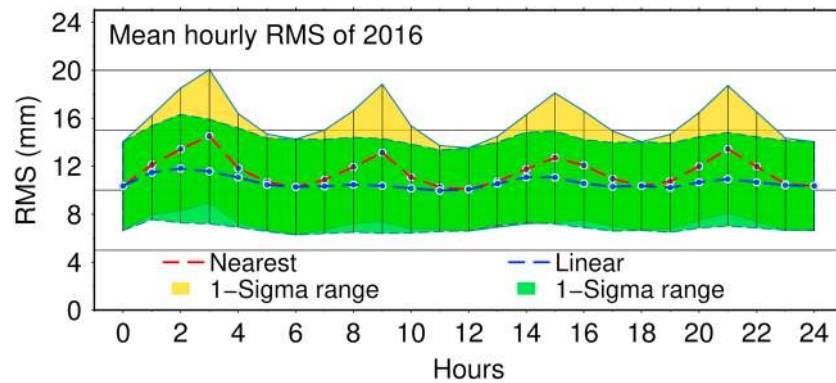
Figure 9. Impact of European Centre for Medium-Range Weather Forecasts (ECMWF) time differences. The ECMWF zenith total tropospheric delays were evaluated with GPS zenith total tropospheric delays using one year of data from 2016 in Central California. The red line represents the mean root-mean-square (RMS) differences using the nearest (in time) data point method with 1-sigma range plotted as yellow shade. The blue line represents the mean RMS differences using linear interpolation to the interferometric synthetic aperture radar observation time, with the 1-sigma range plotted as green shade.

(2003). The differences are greater in the summer and/or over lower altitude flat regions since the average PWV content is higher compared with those in the autumn or over mountain areas. Hence, to better evaluate the impacts of topography variations, the RMS was scaled. We first divided the study region into uniform 1 by 1 km grid cells and computed the RMS differences for each cell using all MODIS samples that were located in that cell during the whole of 2016. Each of the RMS values were then scaled by the average PWV content of the corresponding cell and are displayed in Figure 10d1. The scaled RMS appears to be strongly correlated with the topography (Figure 10d2), with the higher RMS values occurring over mountains and the lower RMS values over lower, flatter areas. The topography variations cause the PWV to be short wavelength in nature, meaning it is challenging to fully model, thus making accurate InSAR atmospheric correction more difficult (e.g., Zebker et al., 1997; Li, Fielding, Cross, & Preusker, 2009; Bekaert, Hooper, et al., 2015). In practice, lower performances are often expected over high topography variation areas.

6. Conclusions

A generic InSAR atmospheric correction model has been developed by using both HRES-ECMWF grid model output and GPS ZTD pointwise observations, tightly integrated using the ITD model to produce atmospheric (tropospheric) correction maps. This model has been implemented into a Generic Atmospheric Correction Online Service (http://ceg-research.ncl.ac.uk/v2/gacos/), which automatically generates correction maps for user requests. The HRES-ECMWF data, available globally and in near real time, provide the basic input of the correction model, which is enhanced using GPS-estimated ZTDs where available, which improve its performance both spatially and temporally. The developed InSAR atmospheric correction model is (i) global and all time useable, including in the presence of clouds; (ii) potentially near real time (5- to 10-hr latency from HRES-ECMWF, while GPS ZTDs can be generated in real time or with much lower latencies); and (iii) robust and easy to implement automatically, with quality control indicators. While the GPS results presented here are postprocessed, Yu et al. (2017) showed that similar ~1-cm ZTD quality can be obtained in real-time mode, and hence can be applied as herein.

The model developed was evaluated using eight globally distributed interferograms of about 250 × 250 km spatial extent in flat and mountainous topographies, midlatitude and near polar regions, monsoon and oceanic climate systems, and with or without GPS networks. The average improvements in terms of phase StdDev resulting from the atmospheric correction maps applied were 47%, 49%, and 54% for GPS, ECMWF, and the integrated corrections, respectively. The corrected InSAR LOS displacements were also compared with the GPS displacements with average RMS improvements for the four interferograms of 55%, 45%, and 63% for GPS, ECMWF and the integrated corrections, respectively. Hence, the integrated model performs the best, with the combination of different data sources increasing the model's reliability, and the displacement StdDev and RMS difference arising for the corrected interferograms considered is approximately 1 cm.
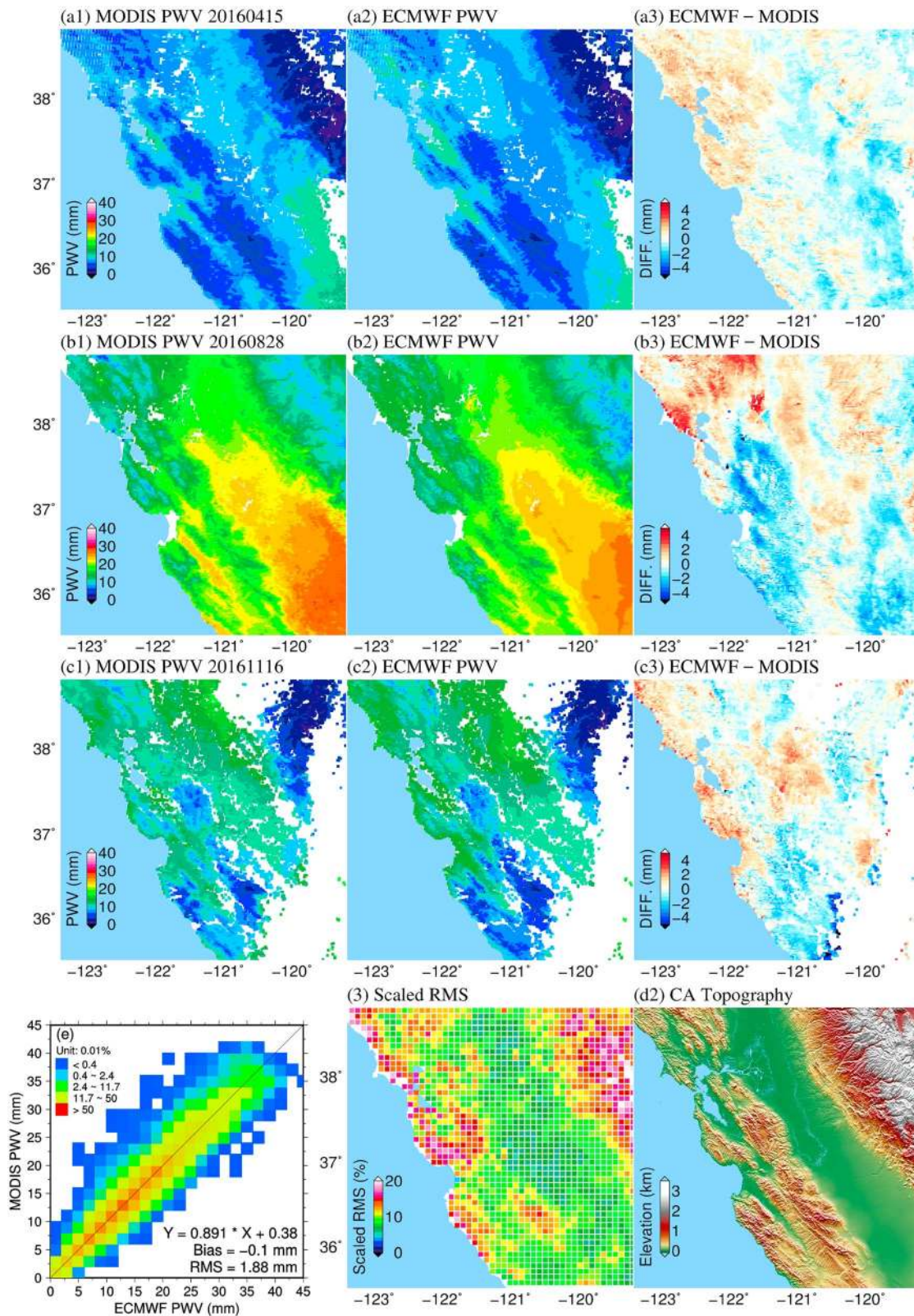
Figure 10. Impact of topography variations. (a–c) Differences in precipitable water vapor (PWV) between Moderate Resolution Imaging Spectroradiometer (MODIS) and European Centre for Medium-Range Weather Forecasts (ECMWF) on cloud free MODIS grid cells on 20160415 (spring), 20161116 (autumn), and 20160828 (summer): (d1) the scaled root-mean-square (RMS) = (averaged RMS of year 2016)/(averaged PWV content of year 2016) for each grid; (d2) the topography; and (e) a linear fit between ECMWF and MODIS PWV for all available pixels of year 2016; the color scale represents the density of occurrence.

A set of performance indicator metrics has also been developed to enable the model's suitability for InSAR atmospheric correction application to be assessed, and we recommend their adoption as indicators to inform users when abnormal conditions occur and give insights of the confidence level of the correction results.

The model developed can be used either on an individual interferogram to identify small amplitude ground movements (e.g., city subsidence and small landslide), or on a series of interferograms for larger-scale plate movements and longer term monitoring (e.g., postseismic or interseismic motion), which allows for temporal filtering to further reduce the residual atmospheric errors and to achieve millimeter per year level displacement StdDev. In most of the currently available InSAR time series packages, two fundamental assumptions are made on the spatial-temporal filtering of the atmosphere that (i) deformation signals are correlated in time (Hooper et al., 2012) and (ii) atmospheric effects are correlated in space but not in time. Since atmospheric effects can be highly correlated with topography, resulting in the spatial trapping of water vapor by topographic features, the second assumption does not hold in most cases. One possible solution is to (i) employ Generic Atmospheric Correction Online Service to apply atmospheric corrections for each interferogram, (ii) utilize the performance indicators to identify the date(s) with poor correction performance, (iii) use the InSAR time series technique demonstrated in Li, Fielding, and Cross (2009) to determine atmospheric phase delays on each date identified in the previous step, and (iv) apply the conventional time series analysis approach to extract the mean deformation rate as well as displacement time series. The bias and uncertainty of the deformation rate can then be quantified by analyzing the systematic and stochastic components of the temporal variation of the atmospheric delay (Fattahi & Amelung, 2015). It is believed that the method is particularly beneficial for InSAR time series over mountain areas as the residual atmospheric errors after correction are more likely to be randomly temporally distributed, which allows an easier minimization through time series analysis, and is an on-going research topic.

References

Béjar-Pizarro, M., Socquet, A., Armijo, R., Carrizo, D., Genrich, J., & Simons, M. (2013). Andean structural control on interseismiccoupling in the North Chile subduction zone. *Nature Geoscience*, 6(5), 1–6. https://doi.org/10.1038/ngeo1802

Bekaert, D. P. S., Hooper, A., & Wright, T. J. (2015). A spatially variable power law tropospheric correction technique for InSAR data. *Journal of Geophysical Research: Solid Earth*, 120, 1345–1356. https://doi.org/10.1002/2014JB011558

Bekaert, D. P. S., Segall, P., Wright, T. J., & Hooper, A. J. (2016). A Network Inversion Filter combining GNSS and InSAR for tectonic slip modeling. *Journal of Geophysical Research: Solid Earth*, 121, 2069–2086. https://doi.org/10.1002/2015JB012638

Bekaert, D. P. S., Walters, R. J., Wright, T. J., Hooper, A. J., & Parker, D. J. (2015). Statistical comparison of InSAR tropospheric correction techniques. *Remote Sensing of Environment*, 170, 40–47. https://doi.org/10.1016/j.rse.2015.08.035

Berrada Baby, H., Golé, P., & Lavergnat, J. (1988). A model for the tropospheric excess path length of radio waves from surface meteorological measurements. *Radio Science*, 23(6), 1023–1038. https://doi.org/10.1029/RS023i006p01023

Beyerle, G. (2009). Carrier phase wind-up in GPS reflectometry. *GPS Solutions*, 13(3), 191–198. https://doi.org/10.1007/s10291-008-0112-1

Blewitt, G., Kreemer, C., Hammond, W. C., & Gazeaux, J. (2016). MIDAS robust trend estimator for accurate GPS station velocities without step detection. *Journal of Geophysical Research: Solid Earth*, 121, 2054–2068. https://doi.org/10.1002/2015JB012552

Bock, O., Keil, C., Richard, E., Flamant, C., & Bouin, M. N. (2005). Validation for precipitable water from ECMWF model analyses with GPS and radiosonde data during the MAP SOP. *Quarterly Journal of the Royal Meteorological Society*, 131(612), 3013–3036. https://doi.org/10.1256/qj.05.27

Boehm, J., Niell, A., Tregoning, P., & Schuh, H. (2006). Global Mapping Function (GMF): A new empirical mapping function based on numerical weather model data. *Geophysical Research Letters*, 33, L07304. https://doi.org/10.1029/2005GL025546

Cavalié, O., Pathier, E., Radiguet, M., Vergnolle, M., Cotte, N., Walpersdorf, A., et al. (2013). Slow slip event in the Mexican subduction zone: Evidence of shallower slip in the Guerrero seismic gap for the 2006 event revealed by the joint inversion of InSAR and GPS data. *Earth and Planetary Science Letters*, 367, 52–60. https://doi.org/10.1016/j.epsl.2013.02.020

Crosetto, M., Tscherning, C. C., Crippa, B., & Castillo, M. (2002). Subsidence monitoring using SAR interferometry: Reduction of the atmospheric effects using stochastic filtering. *Geophysical Research Letters*, 29(9), 1312. https://doi.org/10.1029/2001GL013544

Delacourt, C., P. Briole, and J. Achache (1998), Tropospheric corrections of SAR interferograms with strong topography, Application to Etna, *Geophysical Research Letters*, 25(15), 2849–2852, doi:https://doi.org/10.1029/98GL02112.

Doin, M. P., Lasserre, C., Peltzer, G., Cavalié, O., & Doubre, C. (2009). Corrections of stratified tropospheric delays in SAR interferometry: Validation with global atmospheric models. *Journal of Applied Geophysics*, 69(1), 35–50. https://doi.org/10.1016/j.jappgeo.2009.03.010

Ehret, G., Fix, A., Poberaj, G., Assion, A., Kiemle, C., Hoinka, K. P., & et al. (2000). Low stratospheric water vapor measured by an airborne DIAL. *IGARSS 2000. IEEE 2000 International Geoscience and Remote Sensing Symposium*, 4(D24), 1462–1464. https://doi.org/10.1109/IGARSS.2000.857240

Elliott, J. R., Biggs, J., Parsons, B., & Wright, T. J. (2008). InSAR slip rate determination on the Altyn Tagh Fault, northern Tibet, in the presence of topographically correlated atmospheric delays. *Geophysical Research Letters*, 35, L12309. https://doi.org/10.1029/2008GL033659

Emardson, T. R., Webb, F. H., & Jarlemark, P. O. J. (2002). Analysis of water vapor spatial variability using GPS, InSAR, microwave radiometer, and radiosonde data, *JPL IOM 335–02-1-L*, Jet Propul. Lab., Pasadena, Calif.

Emardson, T. R., & Johansson, J. (1998). Spatial interpolation of the atmospheric water vapor content between sites in a ground-based GPS network. *Geophysical Research Letters*, 25(17), 3347–3350. https://doi.org/10.1029/98GL02504

Emardson, T. R., Simons, M., & Webb, F. H. (2003). Neutral atmospheric delay in interferometric synthetic aperture radar applications: Statistical description and mitigation. *Journal of Geophysical Research*, 108(B5), 2231. https://doi.org/10.1029/2002JB001781

Farr, T. G., Rosen, P. A., Caro, E., Crippen, R., Duren, R., Hensley, S., et al. (2007). The shuttle radar topography Mission. *Reviews of Geophysics*, *45*, RG2004. https://doi.org/10.1029/2005RG000183

Fattahi, H., & Amelung, F. (2015). InSAR bias and uncertainty due to the systematic and stochastic tropospheric delay. *Journal of Geophysical Research: Solid Earth*, *120*, 8758–8773. https://doi.org/10.1002/2015JB012419

Ferretti, A., Prati, C., & Rocca, F. (2001). Permanent scatterers in SAR interferometry. *IEEE Transactions on Geoscience and Remote Sensing*, *39*(1), 8–20. https://doi.org/10.1109/36.898661

Foster, J., Kealy, J., Cherubini, T., Businger, S., Lu, Z., & Murphy, M. (2013). The utility of atmospheric analyses for the mitigation of artifacts in InSAR. *Journal of Geophysical Research: Solid Earth*, *118*, 748–758. https://doi.org/10.1002/jgrb.50093

Fruneau, B., & Sarti, F. (2000). Detection of ground subsidence in the city of Paris using radar interferometry: Isolation of deformation from atmospheric artifacts using correlation. *Geophysical Research Letters*, *27*(24), 3981–3984. https://doi.org/10.1029/2000GL008489

Gendt, G., Dick, G., Reigber, C., Tomassini, M., Liu, Y., & Ramatschi, M. (2004). Near real time GPS water vapor monitoring for numerical weather prediction in Germany. *Journal of the Meteorological Society of Japan*, *82*(1B), 361–370. https://doi.org/10.2151/jmsj.2004.361

Glowacki, T. J., Penna, N. T., & Bourke, W. P. (2006). Validation of GPS-based estimates of integrated water vapour for the Australian region and identification of diurnal variability. *Australian Meteorological Magazine*, *55*, 131–148.

Hanssen, R. (1998). Atmospheric heterogeneities in ERS tandem SAR interferometry.

Hooper, A., Bekaert, D., Spaans, K., & Arikan, M. (2012). Recent advances in SAR interferometry time series analysis for measuring crustal deformation. *Tectonophysics*, *514–517*, 1–13. https://doi.org/10.1016/j.tecto.2011.10.013

Hooper, A., Zebker, H., Segall, P., & Kampes, B. (2004). A new method for measuring deformation on volcanoes and other natural terrains using InSAR persistent scatterers. *Geophysical Research Letters*, *31*, L23611. https://doi.org/10.1029/2004GL021737

Hopfield, H. S. (1971). Tropospheric effect on electromagnetically measured range: Prediction from surface weather data. *Radio Science*, *6*(3), 357–367. https://doi.org/10.1029/RS006i003p00357

Hussain, E., Wright, T. J., Walters, R. J., Bekaert, D., Hooper, A., & Houseman, G. A. (2016). Geodetic observations of postseismic creep in the decade after the 1999 Izmit earthquake, Turkey: Implications for a shallow slip deficit. *Journal of Geophysical Research: Solid Earth*, *121*, 2980–3001. https://doi.org/10.1002/2015JB012737

Jolivet, R., Grandin, R., Lasserre, C., Doin, M. P., & Peltzer, G. (2011). Systematic InSAR tropospheric phase delay corrections from global meteorological reanalysis data. *Geophysical Research Letters*, *38*, L17311. https://doi.org/10.1029/2011GL048757

Jolivet, R., Simons, M., Agram, P. S., Duputel, Z., & Shen, Z. K. (2015). Aseismic slip and seismogenic coupling along the central San Andreas Fault. *Geophysical Research Letters*, *42*, 297–306. https://doi.org/10.1002/2014GL062222

Kouba, J., & Héroux, P. (2001). Precise point positioning using IGS orbit and clock products. *GPS Solutions*, *5*(2), 12–28. https://doi.org/10.1007/PL00012883

Lavers, D. A., Pappenberger, F., Richardson, D. S., & Zsoter, E. (2016). ECMWF extreme forecast index for water vapor transport: A forecast tool for atmospheric rivers and extreme precipitation. *Geophysical Research Letters*, *43*, 11,852–11,858. https://doi.org/10.1002/2016GL071320

Li, Z., Fielding, E. J., & Cross, P. (2009). Integration of InSAR time-series analysis and water-vapor correction for mapping postseismic motion after the 2003 Bam (Iran) earthquake. *IEEE Transactions on Geoscience and Remote Sensing*, *47*(9), 3220–3230. https://doi.org/10.1109/TGRS.2009.2019125

Li, Z., Fielding, E. J., Cross, P., & Muller, J.-P. (2006). Interferometric synthetic aperture radar atmospheric correction: GPS topography-dependent turbulence model. *Journal of Geophysical Research*, *111*, B02404. https://doi.org/10.1029/2005JB003711

Li, Z., Fielding, E. J., Cross, P., & Preusker, R. (2009). Advanced InSAR atmospheric correction: MERIS/MODIS combination and stacked water vapour models. *International Journal of Remote Sensing*, *30*(13), 3343–3363. https://doi.org/10.1080/01431160802562172

Li, Z., Muller, J. P., & Cross, P. (2003). Comparison of precipitable water vapor derived from radiosonde, GPS, and Moderate-Resolution Imaging Spectroradiometer measurements. *Journal of Geophysical Research*, *108*(20), 4651. https://doi.org/10.1029/2003JD003372

Li, Z., Muller, J.-P., Cross, P., Albert, P., Fischer, J., & Bennartz, R. (2006). Assessment of the potential of MERIS near-infrared water vapour products to correct ASAR interferometric measurements. *International Journal of Remote Sensing*, *27*(2), 349–365. https://doi.org/10.1080/01431160500307342

Li, Z., Muller, J. P., Cross, P., & Fielding, E. J. (2005). Interferometric synthetic aperture radar (InSAR) atmospheric correction: GPS, Moderate Resolution Imaging Spectroradiometer (MODIS), and InSAR integration. *Journal of Geophysical Research*, *110*, B03410. https://doi.org/10.1029/2004JB003446

Li, Z. W., Xu, W. B., Feng, G. C., Hu, J., Wang, C. C., Ding, X. L., & et al. (2012). Correcting atmospheric effects on InSAR with MERIS water vapour data and elevation-dependent interpolation model. *Geophysical Journal International*, *189*(2), 898–910. https://doi.org/10.1111/j.1365-246X.2012.05432.x

Liu, J., & Ge, M. (2003). PANDA software and its preliminary result of positioning and orbit determination. *Wuhan University*, *8*(2), 603–609. https://doi.org/10.1007/BF02899825

Lofgren, J. S., Bjorndahl, F., Moore, A. W., Webb, F. H., Fielding, E. J., & Fishbein, E. F. (2010). Tropospheric correction for InSAR using interpolated ECMWF data and GPS Zenith Total Delay from the Southern California Integrated GPS Network, in *2010 IEEE International Geoscience and Remote Sensing Symposium*, pp. 4503–4506, IEEE.

Luzi, G., Pieraccini, M., Mecatti, D., Noferini, L., Guidi, G., Moia, F., & et al. (2004). Ground-based radar interferometry for landslides monitoring: Atmospheric and instrumental decorrelation sources on experimental data. *IEEE Transactions on Geoscience and Remote Sensing*, *42*(11), 2454–2466. https://doi.org/10.1109/TGRS.2004.836792

Massonnet, D., Feigl, K., Rossi, M., & Adragna, F. (1994). Radar interferometric mapping of deformation in the year after the Landers earthquake. *Nature*, *369*(6477), 227–230. https://doi.org/10.1038/369227a0

Nico, G., Tome, R., Catalao, J., & Miranda, P. M. A. (2011). On the use of the WRF model to mitigate tropospheric phase delay effects in SAR Interferograms. *IEEE Transactions on Geoscience and Remote Sensing*, *49*(12), 4970–4976. https://doi.org/10.1109/TGRS.2011.2157511

Onn, F., & Zebker, H. A. (2006). Correction for interferometric synthetic aperture radar atmospheric phase artifacts using time series of zenith wet delay observations from a GPS network. *Journal of Geophysical Research*, *111*, B09102. https://doi.org/10.1029/2005JB004012

Petit, G., & Luzum, B. (2010). IERS Conventions (2010), (IERS Technical Note 36) Frankfurt am Main: Verlag des Bundesamts für Kartographie und Geodäsie, 2010 (179 pp.).

Rocken, C., Anthes, R., Exner, M., Hunt, D., Sokolovskiy, S., Ware, R., et al. (1997). Analysis and validation of GPS/MET data in the neutral atmosphere. *Journal of Geophysical Research*, *102*(D25), 29,849–29,866. https://doi.org/10.1029/97JD02400

Short, N., LeBlanc, A. M., Sladen, W., Oldenborger, G., Mathon-Dufour, V., & Brisco, B. (2014). RADARSAT-2 D-InSAR for ground displacement in permafrost terrain, validation from Iqaluit Airport, Baffin Island, Canada. *Remote Sensing of Environment*, *141*, 40–51. https://doi.org/10.1016/j.rse.2013.10.016

Simons, M., & Rosen, P. A. (2007). Interferometric synthetic aperture radar geodesy. In *Treatise on geophysics* (Vol. 3, pp. 391–446). Amsterdam: Elsevier.

Tachikawa, T., Kaku, M., Iwasaki, A., Gesch, D. B., Oimoen, M. J., Zhang, Z., et al. (2011). *ASTER Global Digital Elevation Model version 2— Summary of validation results*. Sioux Falls: NASA.

Wadge, G., Webley, P. W., James, I. N., Bingley, R., Dodson, A., Waugh, S., et al. (2002). Atmospheric models, GPS and InSAR measurements of the tropospheric water vapour field over Mount Etna. *Geophysical Research Letters*, *29*(19), 1905. https://doi.org/10.1029/2002GL015159

Wang, J., Zhang, L., & Dai, A. (2005). Global estimates of water-vapor-weighted mean temperature of the atmosphere for GPS applications. *Journal of Geophysical Research*, *110*, D21101. https://doi.org/10.1029/2005JD006215

Webley, P. W., Bingley, R. M., Dodson, A. H., Wadge, G., Waugh, S. J., & James, I. N. (2002). Atmospheric water vapour correction to InSAR surface motion measurements on mountains: Results from a dense GPS network on Mount Etna. *Physics and Chemistry of the Earth, Parts A/B/C*, *27*(4–5), 363–370. https://doi.org/10.1016/S1474-7065(02)00013-X

Wessel, P., Smith, W. H. F., Scharroo, R., Luis, J., & Wobbe, F. (2013). Generic mapping tools: Improved version released. *Eos, Transactions American Geophysical Union*, *94*(45), 409–410. https://doi.org/10.1002/2013EO450001

Williams, S., Bock, Y., & Fang, P. (1998). Integrated satellite interferometry: Tropospheric noise, GPS estimates and implications for interferometric synthetic aperture radar products. *Journal of Geophysical Research*, *103*(B11), 27,051–27,067. https://doi.org/10.1029/98JB02794

Yu, C., Li, Z., & Penna, N. T. (2018). Interferometric synthetic aperture radar atmospheric correction using a GPS-based iterative tropospheric decomposition model. *Remote Sensing of Environment*, *204*, 109–121. https://doi.org/10.1016/j.rse.2017.10.038

Yu, C., Penna, N. T., & Li, Z. (2017). Generation of real-time mode high-resolution water vapor fields from GPS observations. *Journal of Geophysical Research: Atmospheres*, *122*, 2008–2025. https://doi.org/10.1002/2016JD025753

Zebker, H. A., Rosen, P. A., & Hensley, S. (1997). Atmospheric effects in interferometric synthetic aperture radar surface deformation and topographic maps. *Journal of Geophysical Research*, *102*(B4), 7547–7563. https://doi.org/10.1029/96JB03804